An Ultra-high Gain Current-fed Universal Auxiliary Power Module for 400V/800V Electric Vehicles

Liyan Zhu
Department of Electrical Engineering and Computer Science
University of Tennessee
Knoxville, TN, USA
liyan@utk.edu

Hua Bai
Department of Electrical Engineering and Computer Science
University of Tennessee
Knoxville, TN, USA
hbai2@utk.edu

Alan Brown
HELLA Electronics Corporation
Northville Township, MI
alan.brown@forvia.com

André Körner
HELLA GmbH & Co. KGaA
Lippstadt, Germany
andre.koerner@forvia.com

***Abstract*—As the counterparts of alternators, the auxiliary power modules (APM) in electric vehicles (EVs) play an irreplaceable role in bridging the high-voltage (HV) propulsion system and low-voltage (LV) auxiliary system. With the increasing demands on fast charging, the HV propulsion system is seeing an involution from 400 V system to 800 V system. To adapt to the trends, the APM also faces the challenge of accepting a wider input voltage range, particularly in EVs with a reconfigurable battery pack. This paper proposed a reconfigurable current-fed dual active bridges (CFDAB) based converter which accepts an ultra-wide-range input from 180V to 900V and an output from 6V to 16V to cover both 400 V and 800 V systems. Topology, operation principles, and simple control to minimize the switching loss are discussed in the paper. A >3 kW prototype with a peak efficiency of 97% was built and tested, which successfully validated the proposed topology and control.**

Keywords— Auxiliary power module, dc-dc converter, electric vehicles, current-fed converter, reconfigurable batteries.

I. INTRODUCTION

The auxiliary power module (APM) is an important part of the charging system in electric vehicles (EVs), which uses the HV system to charge the LV battery and support all LV loads, e.g., the headlights, sensors, power steering systems, and some other critical loads. Two major challenges exist in the APMs design. Firstly, the wide input and output voltage range. The APMs connect HV and LV batteries, and both batteries have a wide voltage range. For example, for an HV battery rated at 400V, the terminal voltage can vary from 180V to 450V[1], and an 800V system has the terminal voltage changing from 500V to 900V[2]. More critically, EVs that are equipped with reconfigurable battery packs to adopt both 400V and 800V charging systems are emerging. The APM inside then has to accept an input voltage from 180V to 900V[3]–[6]. No mention the output voltage also varies from 6V to 16V[7], [8]. A wide voltage range means wide range of the voltage gain. A typical voltage gain from 0.94 to 12.5 is then required to cover the full voltage range, where the voltage gain is defined as input voltage divided by the product of output voltage and transformer turn ratio.

Secondly, the high output current. It will be particularly difficult for an ultra-high-gain converter to deliver high output current across the whole voltage range. Due to the low output voltage, the APM usually suffers the high current stress at the LV side. For instance, a 3.5kW output at 12V yields an output current up to 300A. For the commonly used topologies such as LLC [9]–[11] and DAB [12]–[15], the heavy loads either mean high switching current or unpractically high voltage gain. Some other two-stage designs are able to provide high power and wide voltage gain, but the topology is complex and the cost is high[16], [17].

The literatures proposed multiple topologies for wide-voltage-range applications. However, most of them are designed for the 400 V application only. The voltage gain is still not high enough to cover the 400 V and 800 V reconfigurable system. No mention to alleviate the current stress.

This paper proposed a CFDAB based reconfigurable converter, as shown in Fig. 1. Compared with existing technologies, four major superiorities exhibit:

1. The ultra-high voltage gain. The current-fed port integrates an interleaved buck stage and presents an ultra-wide voltage coverage. The reconfigurable topology further extends the voltage gain and improves the extreme voltage case's efficiency.

2. The low RMS and switching current on the LV side. The current-fed (CF) port has a nature of low switching current when the duty cycles are well controlled. The switching current is only the circulating current to charge the clamp capacitor.

3. Asymmetric current stress on the current-fed port. The CF port presents different rms current on top switches and bottom switches. High-side switches only handle a very low circulating current. This allows an asymmetric hardware design to save costs.

4. CF converter naturally presents a high voltage gain, the proposed reconfigurable topology furtherly extends the voltage range by altering the input port as CF port or VF port.

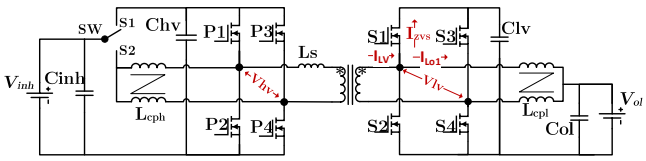

Fig. 1. Proposed reconfigurable CFDAB for the ultra-wide voltage range APM

II. Operation of Reconfigurable CFDAB

The proposed topology is illustrated in Fig. 1. A CF port is equipped on the LV side, while the HV port can be configured as either the voltage-fed (VF) or CF port by the switch SW. The CF port on the LV side helps to reduce the transformer turn ratio and the current stress. The HV port is designed as reconfigurable to extend the voltage range and increase the power capability at the extreme voltage range. The CF port input/output filters L_{CPL} and L_{CPH} are coupled inductors to shrink the size. Chv and Clv are clamp capacitors to provide a stable voltage for the full bridges. The Ls is the leakage inductance of the transformer. V_{inh} is the HV battery voltage and V_{ol} is the LV battery voltage. The voltage applied to the transformer terminals is denoted as V_{hv} and V_{lv}.

A. Operation of CF port

For the LV side CF port, it can be decomposed into a VF full bridge plus an interleaved boost stage, as shown in Fig. 2. For the voltage applied to the HV winding, it is determined by both input voltage *Vinh* and HV side duty cycle *Dh*. However, in the VF mode, the winding terminal voltage is solely determined by *Vinh*. Typical waveforms of transformer terminal voltages, currents and control variables are shown in Fig. 3.

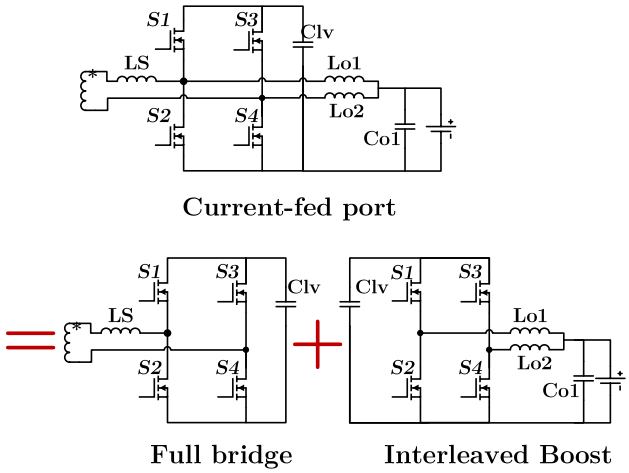

Fig. 2 The decomposition of the LV-side CF port

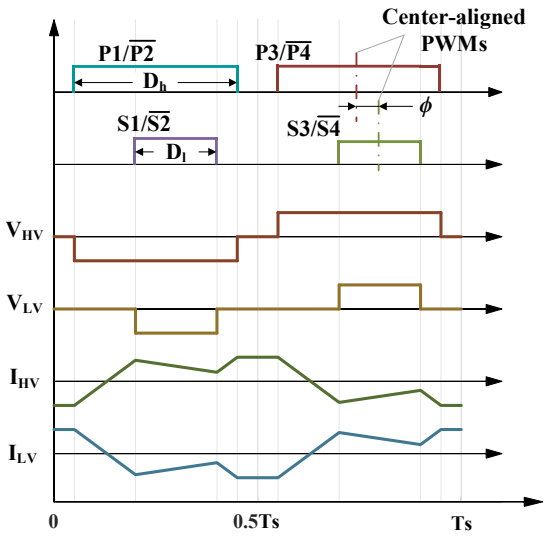

Fig. 3 typical waveforms of CFDAB

Different from the VF port, where the switch-on and switch-off currents are only determined by the transformer current, the switching currents of a CF port are determined by both the transformer current and the coupled inductor current, as illustrated in Fig. 4.

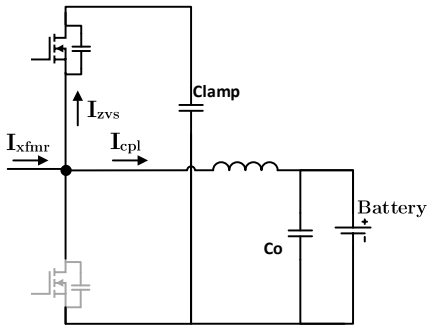

Fig. 4 Switching current of the CF port

The LV side is always a CF port despite the HV side configuration. The operational principles, advantages, and characteristics of the CF port include the following:

1. A CF port on the LV side helps to reduce the transformer turn ratio, thus facilitating the transformer's fabrication. As shown in Fig. 2, the embedded interleaved boost stage boosts the LV battery voltage, thus effectively reducing the transformer turn ratio.

2. The CF port high-side switches (S1, S3) and low-side switches (S2, S4) carry different rms current. The typical current and voltage waveform of the CF port switches are illustrated in Fig. 5. It clearly shows the high-side and low-side switches are undertaking different rms currents. This is particularly beneficial for the high-current LV side since fewer high-current MOSFETs are needed for the high side.

3. The low-side switches carry a much higher load current. However, the switching current is still the same as the high-side switches. This reveals another significant benefit of the CF port, i.e., the switching current can be low regardless of the output

power. More detailed switching current and related operational modes will be discussed later.

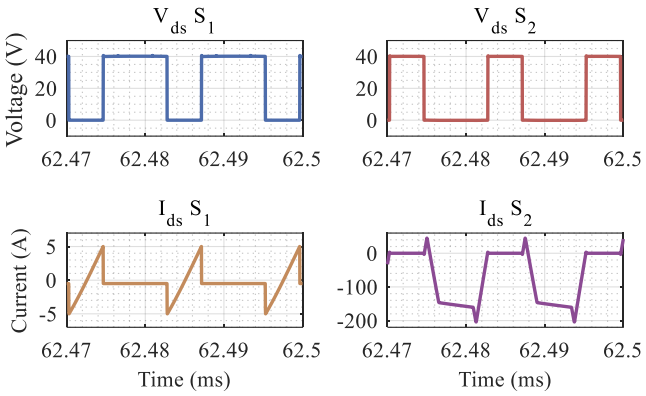

Fig. 5 The typical V_{ds} and I_{ds} of CF port

However, such benefits of decoupled power and switching current is only valid within the boundary of $\phi \leq D_h - D_l$. If the phase shift exceeds the boundary, the switching current of the LV port will increase rapidly with the power, as shown in Fig. 6 and Fig. 7. This is a key operational boundary of the proposed topology, and the design will control the duty cycles to make sure the converter does not exceed the boundary in major operational range.

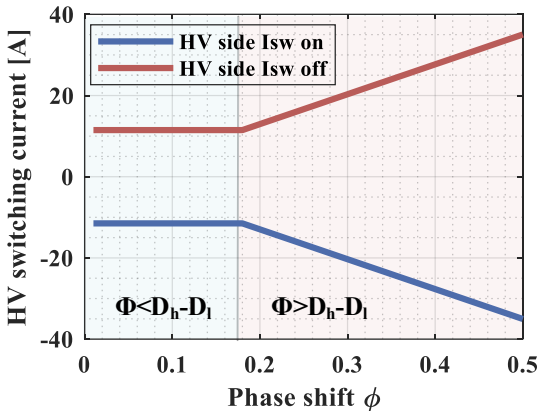

Fig. 6 HV side switching current

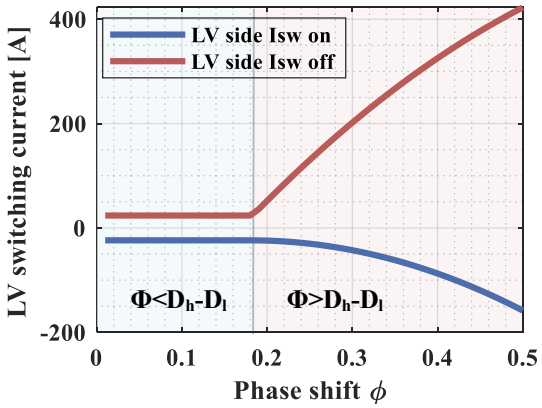

Fig. 7 LV side switching current

B. HV configured as VF Port

When the *SW* shown in Fig. 1 is switched to position S1, the HV port is configured as VF, and the LV side is kept as CF. This configuration will be noted as VF-CFDAB in the paper. The output power of the VF-CFDAB is

$$P_{VF} = \frac{N_t \phi T_s V_{inh} V_{ol}}{L_s} \tag{1}$$

The HV side switching-on and switching-off currents are symmetric, which means the switching-on current equals the negative value of the switching-off current. The switching-on current is

$$I_{VF_{hv-on}} = -\frac{T_s(D_h V_{inh} - N_t V_{ol})}{2L_s} \tag{2}$$

The LV side switching-on and switch-off currents are also symmetric. The switch-on current is

$$I_{VF_{lv-on}} = -\frac{N_t T_s (N_t V_{ol} - D_l V_{inh})}{2L_s} - \frac{T_s V_{ol}(L_{lv} - D_l L_{lv} + D_l M_{lv})}{2(L_{lv}^2 - M_{lv}^2)} \tag{3}$$

where L_{lv} is the self inductance of the LV side coupled inductor L_{CPL}, and M_{lv} is the mutual inductance between two symmetric L_{CPL} windings. It is clear that the overall current consists of both transformer current and coupled inductor ripple current.

C. HV Side Configured as a CF Port

When the switch *SW* shown in Fig. 1 is switched to position S2, the HV port is configured as the CF mode, which will be noted as CF-CFDAB configuration in this paper. The output power of the CF-CFDAB is

$$P_{CF} = \frac{N_t \phi T_s V_{inh} V_{ol}}{D_h L_s} \tag{4}$$

The power has a similar form as VF-CFDAB. The main difference is the involvement of D_h. Meanwhile, in CF-CFDAB the peak voltage on C_{HV} is boosted to V_{inh}/D_h, thus special attention is needed for the voltage constraints when optimizing the duty cycle.

The CF-CFDAB configuration is more complex due to the introduction of an additional coupled inductor. α, β, γ and δ given in (5)~(8) are used to shorten the equations, where L_{hv} is the self inductance of L_{CPH} and M_{hv} is the mutual inductance between L_{CPH} windings.

$$\alpha = \frac{T_s V_{inh}(L_{hv} - D_h L_{hv} + D_h M_{hv})}{2(L_{hv}^2 - M_{hv}^2)} \tag{5}$$

$$\beta = \frac{T_s V_{ol}(L_{lv} - D_l L_{lv} + D_l M_{lv})}{2(L_{lv}^2 - M_{lv}^2)} \tag{6}$$

$$\gamma = \frac{N_t T_s (D_h^2 - 2D_h D_l - 2D_h \phi + D_l^2 - 2D_l \phi + \phi^2)}{8 D_h D_l L_s} \tag{7}$$

$$\delta = \frac{T_s(V_{inh} - N_t V_{ol})}{2L_s} \tag{8}$$

The switch-on and switch-off currents are still symmetrical despite the configuration. The HV port switch-on current is

$$I_{CF\,hvon} = -\alpha - \delta - \frac{N_t \phi T_s V_{ol}}{2D_h L_s} \tag{9}$$

The LV port switch-on current is

$$I_{CF\,lvon} = \frac{D_l N_t T_s V_{inh}}{2D_h L_s} - \frac{N_t^2 T_s V_{ol}}{2L_s} - \beta \tag{10}$$

III. Control for Reconfigurable CFDAB

From (2), it's clear that for the HV side, the zero-voltage - switching (ZVS) turn-on is naturally guaranteed when $D_h > \frac{N_t V_{ol}}{V_{inh}}$, where D_h for the VF mode is physically limited to D_h<0.5. Using this as the boundary condition, the whole voltage range with the expected efficiency map can be divided into the VF range and CF range, as shown in Fig. 8.

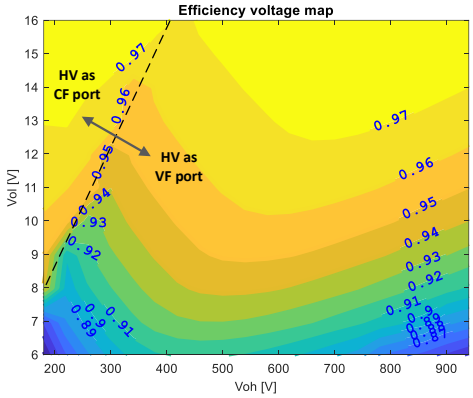

Fig. 8 The boundary of VF/CF mode and estimated efficiency map

As discussed, the power and the switching current are decoupled when $\phi \le D_h - D_l$. Thus to simplify the control and keep the switching current low, this paper will fix $D_h = D_l + \phi$. The boundary condition can then be satisfied. The power is then solely controlled by the phase shift, and D_l can be utilized to control the LV side switching current.

When D_h is set as $D_l + \phi$, both HV side and LV side switching currents are related to the LV side duty cycle D_l. The switching current vs. D_l is illustrated in Fig. 9 and Fig. 10. It is clear that the lowest switching current of the HV side and LV side are happening at different D_l. However, checking the whole duty cycle range, the HV switching current only changes for a few amperes, but the LV side switching current changes up to 100A. Thus, D_l will be used to minimize the LV switching current instead of the HV side.

In addition, figures also indicate the switch-on and switch-off currents have the same aptitude but opposite directions. Thus the switch-off current can not be set to zero. In practice, to achieve ZVS, the switch-on current, or the negative switch-off current must be larger than the boundary current in (11).

$$I_{zvs} = \frac{2Q_{oss}}{T_{db}} \tag{11}$$

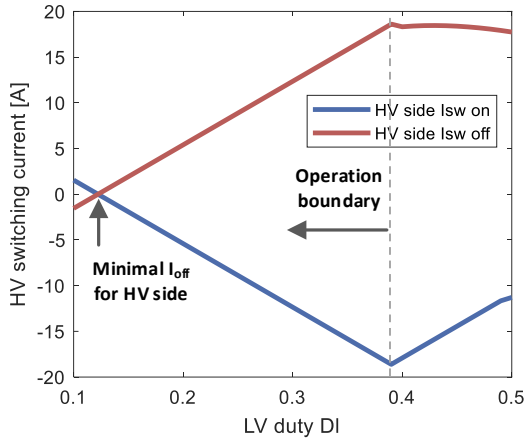

Fig. 9 HV switching current vs. D_l

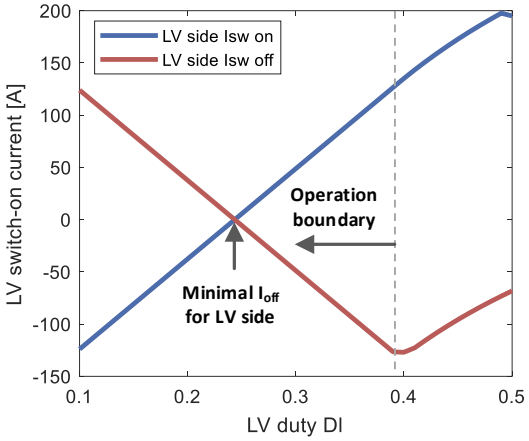

Fig. 10 LV switching current vs. D_l

Then the optimized duty cycle to secure ZVS and minimize the switch-off current is calculated as

$$D_{l_{opt}} = \frac{\frac{T_s V_{ol} N t^2}{2L_s} - \frac{2Q_{lv}}{T_{db}} + \frac{L_{lv} T_s V_{ol}}{2L_{lv}^2 - 2M_{lv}^2}}{\frac{N_t T_s V_{inh}}{2L_s} + \frac{T_s V_{ol}(L_{lv} - M_{lv})}{2L_{lv}^2 - 2M_{lv}^2}} \tag{12}$$

Due to limited computational resources, it is difficult to calculate the optimized duty cycles online. Since the duty is only related to the input and output voltage, it is feasible to do the optimization offline and store results as a look-up table (LUT) for the control usage.

The overall optimization and control flow are summarized as follows: 1) Run the optimization for the LV side switching current and save the result as a look-up table (LUT); 2) Save the boundary HV side duty cycles for ZVS; 3) In the real-time control, select D_l based on input/output voltages from LUT; 3) Regulate the phase for the target power; 4) HV side duty cycle will be set as $D_h = D_l + \phi$. If the calculated D_h is out of the ZVS boundary or reaches the maximal $D_h = 0.5$, keep D_h at the boundary.

IV. Experimental Results

A 3kW prototype is built to test the proposed topology and the control method. The hardware parameters, wide voltage range power capability, efficiency, and loss breakdown are presented in this section.

A. Hardware implementation

Following the design consideration and optimization procedure, the parameters of the prototyped hardware are listed in Table. I.

Table. I Hardware parameters of the prototypes

Input voltage range	180 – 900 V
Output voltage range	6 – 16 V
Max output power	3 kW
HV-side switches	2×C3M0032120K
LV-side switches	2×IRF100P219
Switching frequency	80 kHz
Leakage inductance	42 μH
Magnetizing inductance	540 μH
Transformer turn ratio N_t	12 : 1
Transformers Core	3C95, E65/32/27
HV coupled inductor self inductance	50 μH
HV coupled inductor mutual inductance	35 μH
LV coupled inductor self inductance	10 μH
LV coupled inductor mutual inductance	8 μH
Coupled inductors core	3C95, E65/32/27

B. Power test

The power test covers different input and output voltages. The maximum power is tested up to 3.2 kW at 700 V input and 16 V output. The full voltage range is also tested to cover 6 V to 16 V output and 180 V to 900 V input.

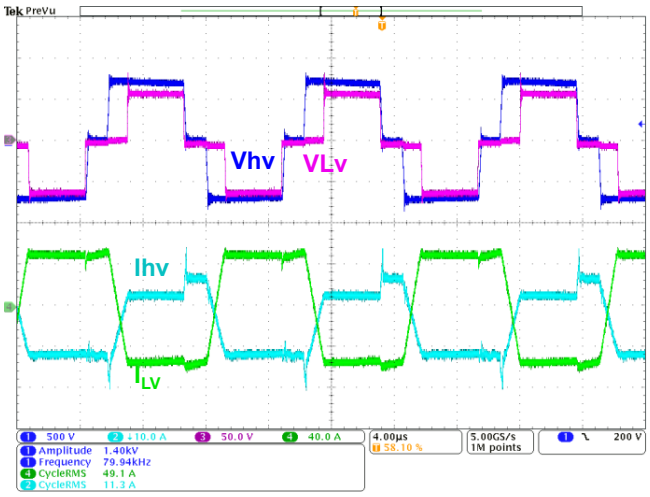

Fig. 11 Test at 700V/16V, 3.25kW

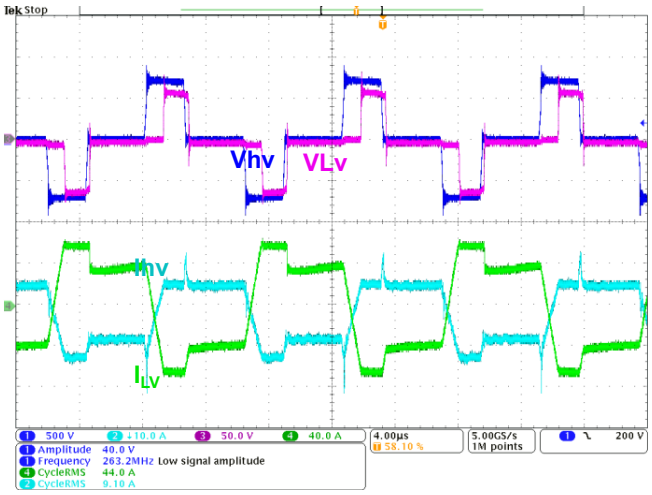

Fig. 12 Test at 700V/6V, 1.6kW

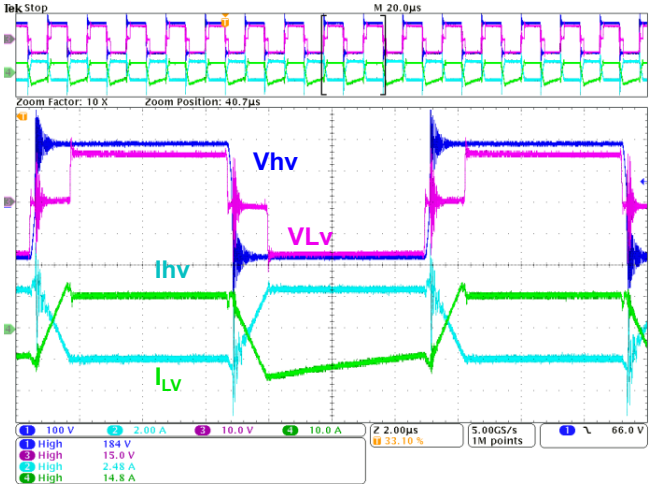

Fig. 13 Test at 180V/6V, 260 W

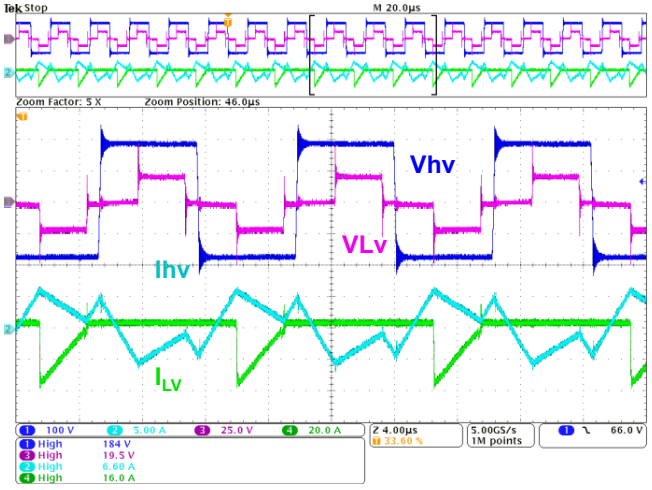

Fig. 14 Test at 180V/16V, 330 W

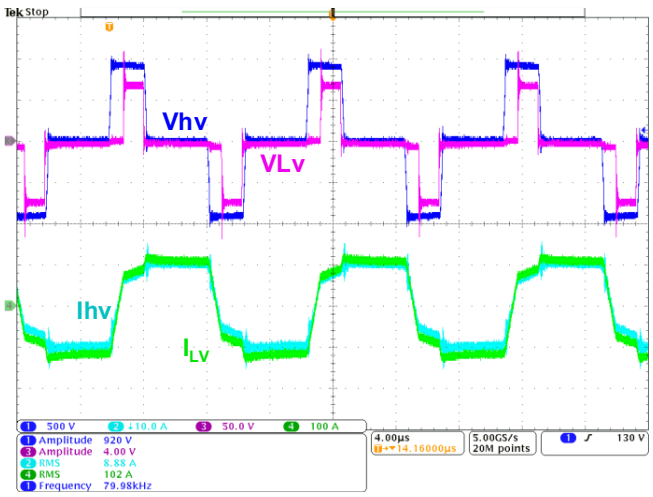

Fig. 15 Test at 900V/6V, 1.1 kW

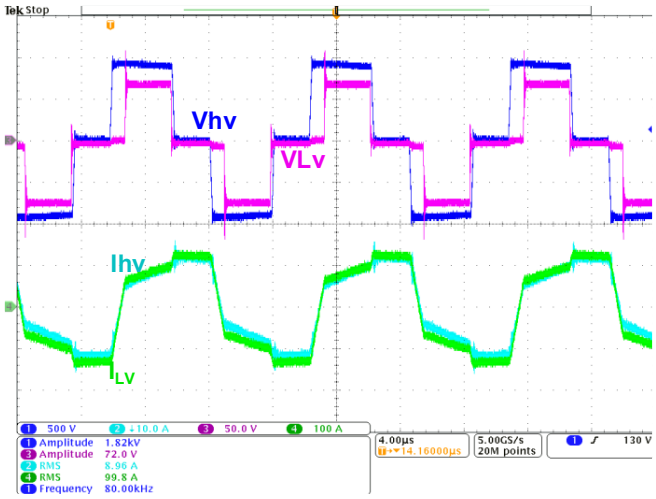

Fig. 16 Test at 900V/16V, 2.6 kW

C. *Efficiency and loss breakdown*

The efficiency is tested under different voltages, as shown in Fig. 17. The peak efficiency is >97% at 1.5kW output. The efficiency curve also indicates the power capability for the corner cases by examining the maximal tested power for each curve. Note that the maximal power is aligned with real-world requirements and constraints. For example, at the low input voltage and high output voltage, the maximum required power is only 500W, which is reasonable given that the HV battery is almost drained and the LV side battery is almost full thereby no need to charge the LV battery with high power. Another case is when the input voltage is high but the output voltage is low. The maximal power is relatively higher at 1.5 kW. Such a requirement also comes from the real application, given the HV battery has a high state of charge (SoC) and can provide enough power, while at the same time the LV battery is almost drained and needs higher charging power.

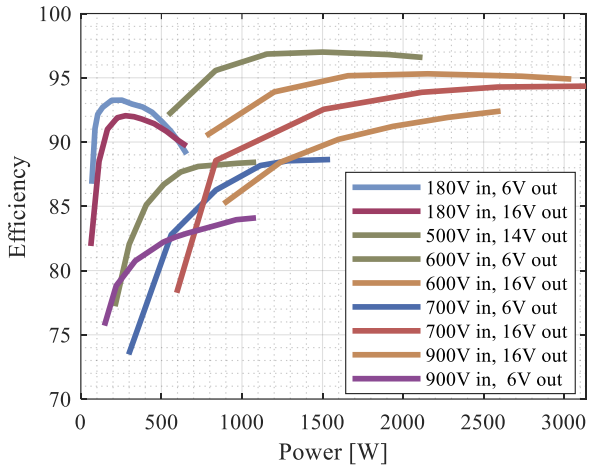

Fig. 17 Efficiency map

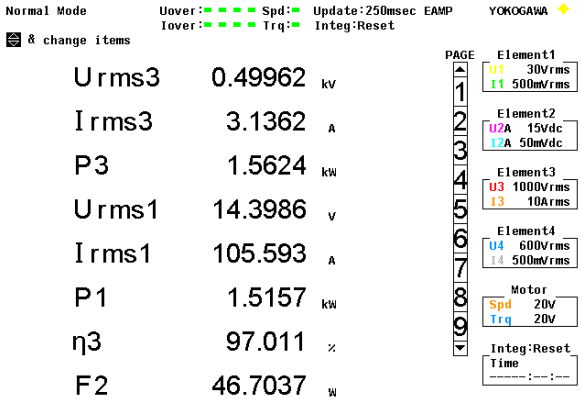

Fig. 18 Peak efficiency of 97% at 500V input/14V output

The loss breakdown is also included. Aligned with what was mentioned early in the paper, the major losses come from the LV side switching losses and conduction losses.

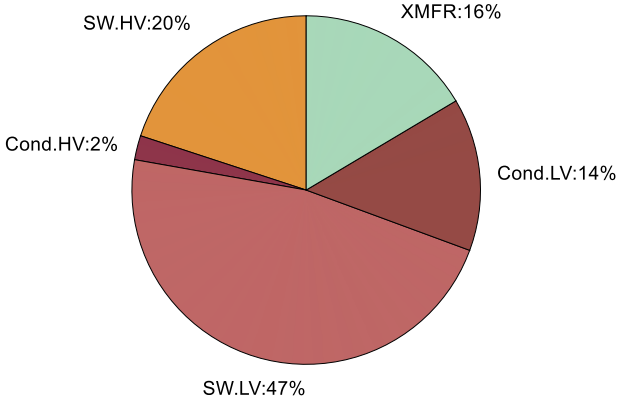

Fig. 19 Loss breakdown at 600V/16V/2.2kW (103 W overall loss)

V. CONCLUSIONS

This paper proposed a reconfigurable APM topology to cover an ultra-wide input and output voltage range. The detailed analytical models to calculate the power and switching current are derived for both VF and CF configurations in two major

operational modes. The corresponding optimization method is proposed for a simple control to minimize the switching losses and secure a full-range ZVS. The power tests have been done to cover 180V to 800V input and 6V to 16V output, with a peak efficiency of 97% and a maximal power of 3.2kW. The test results validated the wide voltage capability and effectiveness of the control, which marks the proposed converter as a promising candidate to power the LV system for the emerging 400V/800V EVs. The proposed technology compared to the existing products and literatures is summarized in Table. II.

Table. II Specifications and performance comparison

Products /prototypes	Input voltage	Output voltage	Peak power	Peak efficiency
UTK [17]	250 – 450 V	10 – 16 V	7.0 kW	96%
CAS-EV [18]	240 – 400 V	10 – 15 V	2.7 kW	94%
BorgWarner [19]	220 – 800 V	11 – 13.5 V	1.2 kW	92%
Eaton [20]	225 – 450 V	6 – 16 V	3.0 kW	94%
Bosch [21]	250 – 475 V	10.5 – 15.5 V	3.6 kW	95%
Vitesco [22]	220 – 450 V	8 – 16 V	3.5 kW	
Bel Power [23]	400 – 800 V	9 – 16 V	4 kW	93%
NCKU [24]	220 – 450 V	9 – 16 V	2.5 kW	97%
Seoul Tech [25]	460 – 780 V	11.5 – 15.1 V	1.2 kW	93%
Queen's [26]	250 – 430 V	9 – 16 V	1.3 kW	96.5%
NUAA [27]	200 – 450 V	9 – 14.4 V	3 kW	94.7%
This work	180 – 900 V	6 – 16 V	3.25 kW	97%

REFERENCES

[1] L. Kostal, L. Schmidhauser, L. Kabel, and R. Bosch, "Voltage Casses for Electric Mobility," 2013.

[2] C. Jung, "Power Up with 800-V Systems: The benefits of upgrading voltage power for battery-electric passenger vehicles," *IEEE Electrification Mag.*, vol. 5, no. 1, pp. 53–58, Mar. 2017, doi: 10.1109/MELE.2016.2644560.

[3] C. Jung, "Power Up with 800-V Systems: The benefits of upgrading voltage power for battery-electric passenger vehicles," *IEEE Electrification Mag.*, vol. 5, no. 1, pp. 53–58, Mar. 2017, doi: 10.1109/MELE.2016.2644560.

[4] I. Aghabali, J. Bauman, P. J. Kollmeyer, Y. Wang, B. Bilgin, and A. Emadi, "800-V Electric Vehicle Powertrains: Review and Analysis of Benefits, Challenges, and Future Trends," *IEEE Trans. Transp. Electrification*, vol. 7, no. 3, pp. 927–948, Sep. 2021, doi: 10.1109/TTE.2020.3044938.

[5] S. Mungekar, A. Dey, and G. Gohil, "High Efficiency Bidirectional DC-DC Converter with Matrix Transformer for Heavy Duty Hybrid Electric Vehicles," in *2020 IEEE Energy Conversion Congress and Exposition (ECCE)*, Oct. 2020, pp. 641–648. doi: 10.1109/ECCE44975.2020.9236243.

[6] J. Engelhardt, J. M. Zepter, T. Gabderakhmanova, G. Rohde, and M. Marinelli, "Double-String Battery System with Reconfigurable Cell Topology Operated as a Fast Charging Station for Electric Vehicles," *Energies*, vol. 14, no. 9, Art. no. 9, Jan. 2021, doi: 10.3390/en14092414.

[7] O. García, L. A. Flores, J. A. Oliver, J. A. Cobos, and J. De La Peña, "Bi-directional dc-dc converter for hybrid vehicles," in *PESC Record - IEEE Annual Power Electronics Specialists Conference*, 2005, vol. 2005, pp. 1881–1886. doi: 10.1109/PESC.2005.1581888.

[8] C. L. Zhu, M. Shen, and M. Obrigkeit, "A high power DC/DC converter designed for single coolant loop hybrid electric vehicle application," in *SAE Technical Papers*, 2010. doi: 10.4271/2010-01-1254.

[9] Y. Jang, M. M. Jovanovic, M. Kumar, J. M. Ruiz, R. Lu, and T. Wei, "Isolated, Bi-directional DC-DC converter for fuel cell electric vehicle applications," *Conf. Proc. - IEEE Appl. Power Electron. Conf. Expo. - APEC*, vol. 2019-March, no. Lv, pp. 1674–1681, 2019, doi: 10.1109/APEC.2019.8722067.

[10] C. Duan *et al.*, "Design of a 2.5kW 400V→M2V high-efficiency DC/DC converter using a novel synchronous rectification control for electric vehicles," in *2013 IEEE Energy Conversion Congress and Exposition, ECCE 2013*, 2013, pp. 1082–1086. doi: 10.1109/ECCE.2013.6646824.

[11] Z. Nie, W. D. Williams, C. Duan, W. Guo, and K. H. Bai, "System optimization of a high-power and high-step-down accessory power module for electric vehicles," in *Conference Proceedings - IEEE Applied Power Electronics Conference and Exposition - APEC*, 2014, pp. 1926–1931. doi: 10.1109/APEC.2014.6803569.

[12] F. Beg, "A Novel Design Methodology for a 1.5 KW DC/DC Converter in EV and Hybrid EV Applications," 2014.

[13] P. Xuewei and A. K. Rathore, "Comparison of bi-directional voltage-fed and current-fed dual active bridge isolated dc/dc converters low voltage high current applications," in *IEEE International Symposium on Industrial Electronics*, 2014, pp. 2566–2571. doi: 10.1109/ISIE.2014.6865024.

[14] L. Zhu, "A novel soft-commutating isolated boost full-bridge ZVS-PWM DC-DC converter for bidirectional high power applications," *IEEE Trans. Power Electron.*, vol. 21, no. 2, pp. 422–429, Mar. 2006, doi: 10.1109/TPEL.2005.869730.

[15] M. R. Ahmed and Y. Li, "A low-cost, high-power-density DC-DC converter for hybrid and electric vehicle applications," in *2019 21st European Conference on Power Electronics and Applications, EPE 2019 ECCE Europe*, Sep. 2019. doi: 10.23919/EPE.2019.8914879.

[16] L. Zhu, H. Bai, A. Brown, and M. McAmmond, "Two-stage vs One-stage Design for A Bidirectional 400V/12V 6kW Auxiliary Power Module in Electric Vehicles," in *2020 IEEE Transportation Electrification Conference & Expo (ITEC)*, Jun. 2020, pp. 1222–1226. doi: 10.1109/ITEC48692.2020.9161459.

[17] L. Zhu, H. Bai, A. Brown, and M. McAmmond, "Design a 400 V–12 V 6 kW Bidirectional Auxiliary Power Module for Electric or Autonomous Vehicles With Fast Precharge Dynamics and Zero DC-Bias Current," *IEEE Trans. Power Electron.*, vol. 36, no. 5, pp. 5323–5335, May 2021, doi: 10.1109/TPEL.2020.3028361.

[18] S. E. Industries, "Downsizing of In-vehicle DC/DC Converters with GaN Devices," p. 6.

[19] "Gen5 High Voltage DC/DC," p. 2.

[20] "eaton-dcdc-converter-data-sheet-brochure-emob0008-en-us.pdf." Accessed: Oct. 18, 2022. [Online]. Available: https://www.eaton.com/content/dam/eaton/products/emobility/power-electronics/dc-dc-converters/eaton-dcdc-converter-data-sheet-brochure-emob0008-en-us.pdf

[21] "High-voltage DC/DC converter generation 3evo." https://www.bosch-mobility-solutions.com/en/solutions/power-electronics/high-voltage-dc-dc-converter-generation-3evo/ (accessed Oct. 18, 2022).

[22] "Vitesco Technologies - High Voltage DC/DC Converter - 4th Generation." https://www.vitesco-technologies.com/en-us/products/high-voltage-dc-dc-converter-4th-generation (accessed Oct. 19, 2022).

[23] "700DNC40-12 - 4000W, 12V, DC-DC HEV Down Converter | Bel Fuse." https://www.belfuse.com/product-detail/power-solutions-custom-value-added-solutions-emobility-700dnc40-down-converter?navCategory=eMobilityDcdcConverters (accessed Oct. 19, 2022).

[24] C.-Y. Chen, T.-J. Liang, K.-F. Liao, K.-H. Chen, and Y.-H. Yeoh, "Design and Implementation of Two-Stage Boost and Full-Bridge Resonant Converter for Wide-Range APMs," in *2021 IEEE International Future Energy Electronics Conference (IFEEC)*, Nov. 2021, pp. 1–6. doi: 10.1109/IFEEC53238.2021.9662017.

[25] H. P. Kieu, D. Lee, S. Choi, and S. Kim, "A 700kHz 800V/14V GaN-based DC-DC Converter with optimized Integrated Transformer for Electrical Vehicles," in *2021 IEEE Energy Conversion Congress and Exposition (ECCE)*, Oct. 2021, pp. 5549–5553. doi: 10.1109/ECCE47101.2021.9595023.

[26] Y. Chen, W. Liu, A. Yurek, X. Zhou, B. Sheng, and Y.-F. Liu, "Design and Optimization of A High Power Density Low Voltage DC-DC Converter for Electric Vehicles," in *2020 IEEE Energy Conversion Congress and Exposition (ECCE)*, Oct. 2020, pp. 1244–1251. doi: 10.1109/ECCE44975.2020.9235889.

[27] X. Xu, Y. Zhang, L. Zhu, H. Yu, Y. Zhang, and H. Wu, "A High Step-down DC-DC Converter with Matrix-Transformer and Wide Voltage Gain for Vehicle Power Supply Applications," in *2019 22nd International Conference on Electrical Machines and Systems (ICEMS)*, Aug. 2019, pp. 1–6. doi: 10.1109/ICEMS.2019.8922407.